A high energy 3V lithium-ion capacitor synthesized via electrostatic spray deposition

Richa Agrawal[1], Chunhui Chen[1], Samantha Dages[1] and Chunlei Wang[1,2,3*]

[1]*Department of Mechanical and Materials Engineering, Florida International University,*
10555 W Flagler St, Miami, FL 33174, USA
[2]*Advanced Materials Engineering Research Institute (AMERI), Florida International University,*
10555 W Flagler St, Miami, FL 33174, USA
[3]*Center for the Study of Matter at Extreme Conditions (CeSMEC), Florida International University,*
10555 W Flagler St, Miami, FL 33174, USA

[*]Corresponding author: E-mail: richaagrawal1017@gmail.com

Received: 10 September 2016, Revised: 26 October 2016 and Accepted: 20 November 2016

DOI: 10.5185/amlett.2017.7098
www.vbripress.com/aml

Abstract

Reduced graphene oxide-carbon nanotube (rGO-CNT) and anatase TiO_2-$Li_4Ti_5O_{12}$ (ATO-LTO) composite electrodes were synthesized via electrostatic spray deposition (ESD) and analyzed as cathode and anode vs. lithium, respectively. The rGO-CNT and ATO-LTO electrodes were able to deliver discharge capacities of ca. 63 $mAhg^{-1}$ and 95 $mAhg^{-1}$, respectively for a current rate of 0.1 Ag^{-1} with superior rate capability and cycle stability. Post electrode analyses, lithium-ion hybrid electrochemical capacitors (Li-HEC) were constructed comprising a prelithiated ATO-LTO anode and an activated rGO-CNT cathode in a carbonate based 1M $LiPF_6$ salt electrolyte. The Li-HEC cells were stable for a cell potential of 0.05-3V and were able to deliver a maximum gravimetric energy density of 33.35 $Whkg^{-1}$ and a maximum power density of 1207.4 Wkg^{-1}, where the cell parameters were normalized with the total mass of the anode and cathode active materials. Furthermore the Li-HEC cells were able to retain ~77% of the initial capacity after 100 cycles. The superior Li-HEC performance is attributed to the utilization of a prelithiated lithium-intercalating anode and a double layer cathode in an asymmetric configuration. The feasibility of using a low-cost, facile process like ESD was therefore shown to produce high performance Li-HECs. Copyright © 2017 VBRI Press.

Keywords: Anatase TiO_2, graphene, carbon nanotubes, lithium-ion capacitors, electrostatic spray deposition.

Introduction

In order to keep up with the demands of the ever evolving technology and the automotive industry, developing high performing energy storage devices is extremely crucial. At the heart of electrochemical energy storage devices are electrochemical capacitors (ECs), which essentially bridge the gap between electrolytic capacitors and secondary batteries with high gravimetric power densities (~10$kWkg^{-1}$) and moderate energy densities (<10$Whkg^{-1}$). However, in order to expand the applicability of ECs, one of the critical factors that requires immediate attention is their relatively low energy density. In the wake of addressing this shortcoming of ECs, the concept of lithium ion battery (LIB) and EC hybridization has gained significant scientific attention in recent years. In practice, battery and capacitor hybridization can be achieved at both external and internal levels. As noted by Cericola et al [**1**], external hybridization involves hardwiring of the two devices in either serial or parallel arrangement, whereas internal hybridization in essence is *hybridization within the device itself*. Similar to the external setup, internal hybridization can be carried out in both serial and parallel arrangements. The internal serial configuration comprises a pristine redox battery-type electrode along with a counter double layer capacitive cathode; whereas the internal parallel arrangement consists of bi-material electrodes, in which both redox and double layer materials coexist within one electrode. One of the first reports on nonaqueous internal hybrids was documented by Amatucci *et al.* in 2001 [**2**], where they used $Li_4Ti_5O_{12}$ as the negative lithium intercalating electrode and activated carbon as the double layer electrode; the reported device was able to deliver a gravimetric energy density of 25$Whkg^{-1}$. Since then many other systems with lithium-intercalating materials including graphite [**3, 4**], $Li_4Ti_5O_{12}$ [**5, 6**], $LiFePO_4$ [**7**], $LiMn_2O_4$ [**8**], TiO_2 [**9-11**], and double layer materials including activated carbon [**2, 5, 6**], and graphene [**8, 12**] have been investigated.

Graphene, the one-atom thick sheet of sp^2 hybridized carbon atoms is considered ideal for double layer capacitive charge storage owing to its high theoretical specific surface area (~2600 m^2/g), exceptional electronic conductivity and superior mechanical strength [**13**].

However, one of the major shortcomings of graphene is sheet aggregation and restacking, which significantly reduces the effective accessible surface area for the electrolyte ions, which ultimately deteriorates the cell performance. One of the strategies to minimize the graphene sheet restacking is the addition of "nanospacers" such as CNT [**14, 15**]. Incorporating CNT into the graphene matrix not only allows for a larger accessible surface area but also enhances the electrical conductivity. Furthermore, the addition of CNT nanofillers has shown improvement in the mechanical robustness of different composites [**16**]. From our previous studies [**14**], microsupercapacitors fabricated with reduced graphene oxide-carbon nanotube (rGO-CNT) composites with a gravimetric composition of 90% rGO and 10% CNT exhibited exceptional power handling with a RC time constant of only 4.8 ms. The further addition of CNT enhanced the power handling but exhibited a negative impact on the specific capacitance of the device [**14**]. Therefore rGO-CNT composite electrodes with the same composition were chosen for the lithium hybrid electrochemical capacitor (Li-HEC) fabrication for this study. To couple the rGO-CNT electrode, an anatase TiO_2-$Li_4Ti_5O_{12}$ (ATO-LTO) anode was chosen. TiO_2 (TO) with a maximum theoretical capacity of 335 $mAhg^{-1}$ (for x=1 for Li_xTiO_2) [**17**], is a competitive alternative to graphite-based anodes, which exhibit a theoretical capacity of 372 $mAhg^{-1}$. One of the disadvantages of graphite is the low lithium intercalation potential (~0.1V vs Li/Li^+). Such low operating potentials are very close to lithium plating and can promote dendritic lithium growth, which can result in catastrophic cell short-circuiting. Both TO and LTO intercalate lithium at much higher potentials ~1.4-1.8V [**17**] and ~1.55V vs. Li/Li^+ [**18**], respectively, which are much higher than graphite operating potential. Among the three most sought after TO polymorphs including anatase, bronze and rutile, anatase is considered an ideal host for lithium-ion storage given the highly distorted edge-sharing TiO_2 octahedra arrangement, which facilitates lithium insertion and extraction [**19, 20**]. Furthermore the very low volumetric strain (~4%) in ATO lattice during cycling is ideal for cycle longevity [**20**]. Furthermore, titania has superior electrical conductivity and lithium diffusivity than LTO [**21, 22**] and faster lithium insertion/extraction can help realize higher rate batteries than LTO alone. In other reports, TO-LTO composites have shown enhancement in lithium diffusion, improved charge-transfer kinetics along with better electronic conductivity [**23**].

The electrodes used for the Li-HEC construction for this study were created via electrostatic spray deposition (ESD) technique. The ESD process is a low energy electrohydrodynamic spraying technique in which a precursor solution disintegrates into an aerosol spray upon the application of a high voltage between a metal nozzle and a substrate [**24-27**]. The desired precursor solution is fed through a syringe pump via a nozzle connected to a high potential source, whereas the substrate is grounded [**24**]. The aerosol formed by the charged droplets is attracted to the heated substrate leading to simultaneous solvent evaporation and chemical reactions, leaving behind a thin film [**26**, **27**]. The advantages of ESD over other thin film production methods include the feasibility of operation in ambient atmosphere at desired temperatures without the need of vacuum, which makes it both cost-effective and facile in terms of operation [**25**]. Both polycrystalline phases as well as composite materials can be synthesized via ESD by adjusting parameters such as the applied potential, substrate temperature, substrate-nozzle distance, nozzle geometry, precursor solution flow rate and composition [**26-28**]. One of the very attractive features of ESD is the ability to tailor the morphology of the film by fine tuning the deposition parameters. A host of morphologies have been reported using ESD including dense, fractal, reticular, sponge-like, and porous [**26, 27**]. The feasibility of creating high-surface area porous and homogeneous synthetic films makes ESD especially suitable for energy-storage applications. Several works have documented the use of ESD based films for energy storage systems including both lithium-ion batteries and electrochemical capacitors [**26, 27, 29-30**]. The ESD based rGO-CNT and the ATO-LTO electrodes, synthesized in this work were able to deliver discharge capacities of ~63 $mAhg^{-1}$ and 95 $mAhg^{-1}$, respectively at a current density of 0.1Ag^{-1} with good reversibility. The Li-HEC cells constructed with the rGO-CNT and ATO-LTO electrodes were stable for a cell potential of 0.05-3.0V and were able to deliver a high discharge capacity of ~32 $mAhg^{-1}$ at a current rate of 0.1 Ag^{-1} with excellent rate characteristics and reversibility. Furthermore, the hybrid electrochemical cells were able to deliver a maximum gravimetric energy density of 33.35 $Whkg^{-1}$ and a maximum power density of 1207.4 Wkg^{-1}, with specific energy ranging between 33.35-15.09 $Whkg^{-1}$ at power densities of 83.55-1207.4 Wkg^{-1}. All the cell parameters were normalized with the total anode and cathode active material masses. Additionally, the Li-HEC cells were able to retain a capacity of ~77% after 100 cycles. Therefore, the use of a simple and cost-effective process such as ESD was demonstrated in order to construct high energy Li-HECs with good power handling capability.

Experimental

Material Synthesis

Cathode preparation: For the rGO-CNT cathode, the raw materials were single layer graphene oxide (GO) and carboxyl-functionalized multi-walled carbon nanotubes (MWCNT-COOH). Both the materials were procured from Cheap Tubes Inc. (USA). GO and CNT were first dissolved in 1, 2-propanediol (Sigma Aldrich) in a concentration of 1 $mgml^{-1}$ and were then ultrasonicated for thorough dispersion for 1h. After sonication, the suspension was used immediately for ESD on stainless steel substrates preheated at 250°C. The GO and CNT were used in a gravimetric mass ratio of 9:1, which was selected based on the optimum composition based on our previous works [**14**]. The flow rate was kept between 4-6 $mlhr^{-1}$ at a potential of 5-7 kV and the deposition was carried out for 4 hours. The electrodes were then directly used for material and electrochemical characterization without adding any binders or conducting additives.

Anode preparation: The ATO-LTO anodes were prepared using lithium acetate (Sigma Aldrich) and titanium butoxide (Sigma Aldrich) in a molar ratio of 4:5, respectively in ethyl alcohol and butyl carbitol (4:1 v:v). The solution was directly used as the precursor and deposited on a preheated nickel foam substrate using ESD. The substrate was preheated at 250ºC and the precursor solution flow rate was kept between 1-2 mlhr^{-1}. The potential was kept between 5-7 kV and the distance between the needle and the substrate was approximately 3 cm. The deposition was carried out for 2 h. Post ESD deposition, the substrates with ESD films were calcined in an argon atmosphere in a Lindberg alumina tube furnace at a temperature of 750ºC for 2 h. After the calcination process, the films were allowed to cool down to room temperature and thereafter were directly used for electrochemical characterization without any further treatment or addition of binders or conducting additives.

Material characterization

The crystallinity of the as-deposited and calcined anode powders was studied using a Siemens 5000D X-ray Diffractometer with Cu Kα radiation. Further crystallographic studies on the anode powders calcined at 750ºC were carried out using a Philips CM-200 200KeV Transmission Electron Microscope (TEM). The morphology of the as-deposited and calcined anode films and the rGO-CNT cathode films was characterized using a JEOL SEM 6330F Field Emission Scanning Electron Microscope (FE-SEM) in the secondary electron imaging (SEI) mode. To characterize GO functionalization and reduction, Fourier transform-infrared spectroscopy (FT-IR) was carried out using a JASCO FT-IR 4100 spectrometer.

Electrochemical characterization

The electrochemical characterization was carried out in CR-2032 type coin cells. In order to characterize the electrode performance versus Li/Li$^+$, the rGO-CNT and the ATO-LTO electrodes were first assembled in half-cells as working electrodes with a lithium foil serving both as the counter and reference electrode. 1.0M lithium hexafluorophosphate ($LiPF_6$) in ethylene carbon (EC): diethyl carbonate (DEC) in a volume ratio of 1:1 was used as the electrolyte, and a Celgard 2400 polypropylene (Charlotte, NC, USA) film was used as the separator. The cells were assembled in an argon-filled glove box (VAC Nexus I, Hawthorne, CA, USA) with O_2 level < 1ppm. Cyclic voltammetry (CV) studies on both rGO-CNT and ATO-LTO electrodes were carried out using a Bio-logic versatile multichannel potentiostat (VMP3) whereas galvanostatic charge-discharge cycling, rate performance and cycle life testing were carried out using a NEWARE BTS-610 Battery Test System (Shenzhen, China). The full hybrid cells comprising the rGO-CNT cathode and ATO-LTO anode were assembled after prelithiating the ATO-LTO anode for 5 cycles and after obtaining the activation of the rGO-CNT electrode for ~100 cycles. For the full cell systems the electrolyte was 1.0M lithium hexafluorophosphate ($LiPF_6$) in ethylene carbon (EC): diethyl carbonate (DEC) in a volume ratio of 1:1, with a Celgard 2400 propylene film separator. Similar to the half-cell assembly, the full cell assembly was carried out in CR-2032 type coin cells.

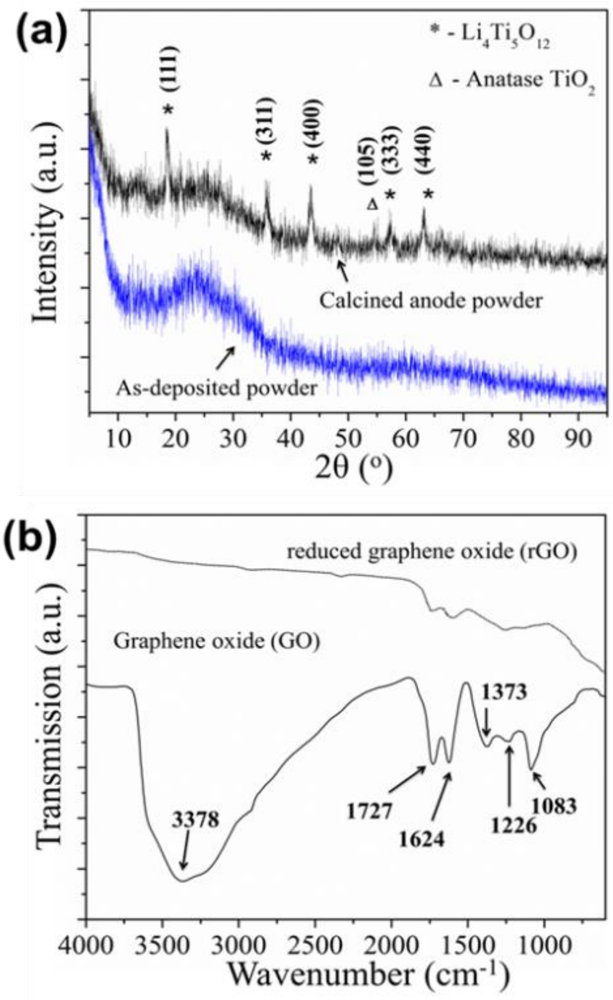

Fig. 1. (a) The XRD pattern of the as-deposited and calcined anode powders, (b) The FTIR pattern of the GO and ESD based rGO.

Results and discussion

The XRD patterns of the as-deposited and anode powders calcined at 750ºC are shown in **Fig. 1a**. As evident, the as-deposited powder exhibits no discernable peaks whereas the diffraction data from the calcined powder validates the presence of both LTO and anatase TiO_2 phase. The peaks at 18.3º, 35.5º, 43.2º, 57.2º and 62.8º correspond to (111), (311), (400), (333) and (440) planes from LTO (JCPDS card number 00-049-0207) whereas the peak at 53.8º corresponds to (105) plane from anatase TiO_2 (JCPDS card number 00-021-1272). The FTIR pattern of the GO powder and the ESD based rGO film is depicted in **Fig. 1b**. The broad absorption peak centered around 3378 cm^{-1} in the GO powder, which signals the presence of hydroxyl groups [**14, 31**] and water is substantially reduced in the rGO pattern. The other significant peaks present in the GO powder are signaled at 1727 cm^{-1}, 1624 cm^{-1}, 1373 cm^{-1}, 1226 cm^{-1}, and 1083 cm^{-1} are attributed to C=O stretching [**31**], aromatic C=C stretching [**32**], carboxyl [**33**], epoxide C-O-C or phenolic C-O-H stretching vibrations [**33**], C-O stretching in epoxy or alkoxy groups [**33**], respectively. It is worth noting that the peak intensity from the groups that signal the presence of oxygen and water are substantially mitigated in the rGO spectrum.

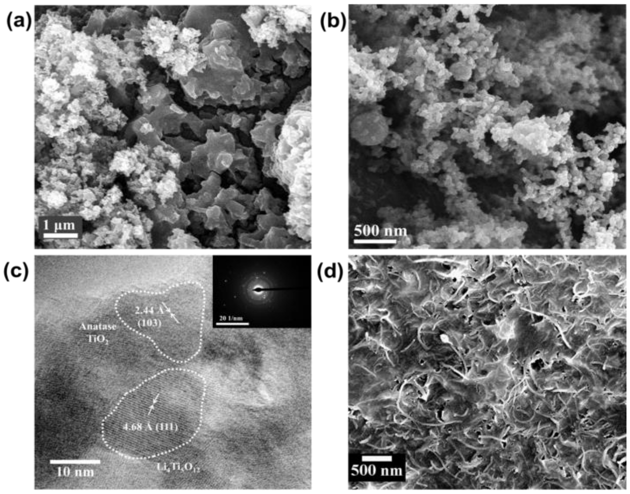

Fig. 2. Morphology of the as-deposited (a) and calcined (b) ATO-LTO films, (c) typical TEM micrograph of the calcined ATO-LTO powder, the inset shows the SAED pattern, (d) Top view of the rGO-CNT cathode.

Fig. 2a and **2b** display the SEM images of the as deposited ESD and calcined ATO-LTO films, respectively. Prior to the thermal treatment, the film particles are mostly flaky, whereas upon the calcination, the particles become more circular with no appreciable change in size. The TEM micrograph of the ATO-LTO powder is shown in **Fig. 2c** and the SAED pattern is shown as the inset. The TEM studies confirmed the presence of both anatase TiO_2 and LTO. The anatase-TiO_2 phase with a d-spacing of 3.50 Å, 2.23 Å, 1.86 Å, 1.54 Å, and 1.19 Å had (hkl) orientations of (101), (112), (200), (213), and (008), respectively, whereas the LTO with d-spacings of 1.25 Å, 1.19 Å, and 1.09 Å and (hkl) orientation of (622), (444), and (731), respectively. The top view of the rGO-CNT electrode is shown in **Fig. 2d**. As evident, the electrode morphology was porous and loose; porous morphology is ideal for double-layer charge storage mechanism and allows for high rate capability realization.

Electrochemical characterization

rGO-CNT half-cell: The cyclic voltammograms at different scan rates of the rGO-CNT composite electrode are shown in **Fig. 3a**. The shape of the curves is typical of a double layer capacitor with no discernable redox peaks. A very interesting phenomenon was observed in **Fig. 3b**; the discharge capacity of the rGO-CNT cathode steadily increased until around the first 60 cycles and then stabilized. The capacity enhancement could be a result of electrochemical activation of the active material and has been reported for graphene based devices in other reports [**14, 34**]. **Fig. 3c** shows the galvanostatic charge-discharge curves of the rGO-CNT composite after the electrochemical activation. The curves are mostly triangular in shape as expected for surface charge storage mechanism. The iR drops however were quite significant at higher current densities, which could be a result of the relatively high resistivity of the composite resulting from the remnant oxygen-containing groups present in the rGO. **Fig. 3d** shows the rate capability of the rGO-CNT composite. The capacity is stable as noted for a step size of 20 cycles for each current rate and almost all of the capacity is recovered when the cell was cycled from 3.2 Ag^{-1} to 0.1 Ag^{-1}. Discharge capacities of ca. 63 $mAhg^{-1}$, 55 $mAhg^{-1}$, 50 $mAhg^{-1}$, 43 $mAhg^{-1}$, 32 $mAhg^{-1}$, and 18 $mAhg^{-1}$are noted for current rates of 0.1 Ag^{-1}, 0.2 Ag^{-1}, 0.4 Ag^{-1}, 0.8 Ag^{-1}, 1.6 Ag^{-1}, and 3.2 Ag^{-1} respectively. The discharge capacities are reported from the last cycle of the respective current rate.

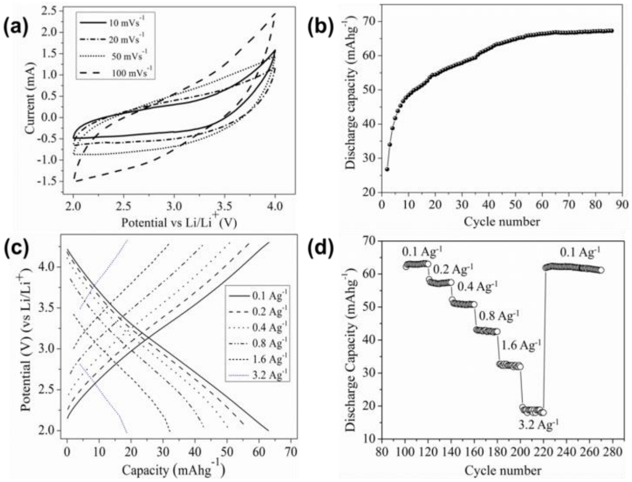

Fig. 3: (a) Cyclic voltammograms of the rGO-CNT composite electrode for different scan rates between a potential of 2.0-4.0V (vs. Li/Li^+), (b) discharge capacity of the rGO-CNT composite for the first ~90 cycles at a current density of 0.1Ag^{-1}, (c) typical charge-discharge curves of the rGO-CNT electrode at different current densities, (d) rate capability of the rGO-CNT composites.

ATO-LTO half cell: The CV curves of the ATO-LTO composite electrodes for the first five cycles at a scan rate of 0.2 mVs^{-1} are shown in **Fig. 4a**. In the first cycle, in the cathodic branch of the scan, two peaks were observed at 1.62V vs. Li/Li^+ and 0.7V vs. Li/Li^+, whereas in the anodic branch one major peak at 2.21V vs. Li/Li^+ was observed. The peak at 0.7V disappeared in the subsequent cycles and is ascribed to the possible solid electrolyte interphase (SEI) formation. The redox peak pair appearing at 1.62V and 2.21V is attributed to the lithium insertion and extraction in ATO. The CV of the ATO-LTO composite at different scan rates is shown in **Fig. 4b**. As evident the peaks shifted upon the application of a higher scan rate. The inset depicts the relationship between the square root of the scan rate and the respective anodic peak current and a linear correlation between the two parameters is established. This indicates the predominance of redox based reactions for the anode based on the Randles–Sevcik equation [**35**]. It should be noted that no discernable activity of LTO is detected in the CV curves, which indicates that ATO is the primarily active electrochemical phase in the composite. The possible reason for no noticeable LTO electrochemical activity could be the competitive crystal growth during the calcination process, which could have resulted in trace LTO amounts. Similar phenomenon, where one of the phases is predominantly electrochemically active in the composite, has been reported in other works [**36, 37**]. **Fig. 4c** shows the charge discharge curves of the first and second cycles of the ATO-LTO composite at a current density of 0.1 Ag^{-1}. Two humps centered at1.62V and 2.21V are observed which are consistent with the CV ATO insertion/extraction redox pair. It should be noted that the first discharge capacity of the composite is ~267 $mAhg^{-1}$ whereas the first charge capacity is ~127 $mAhg^{-1}$ which results in a coulombic efficiency of ~47% resulting in an irreversible capacity loss of 140 $mAhg^{-1}$, which possibly is a result of the SEI formation.

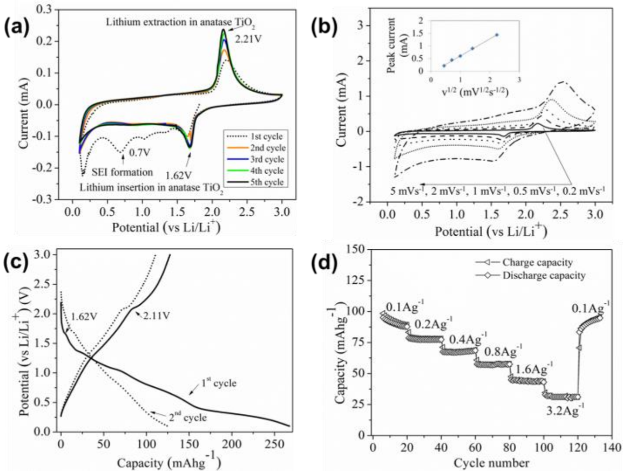

Fig. 4: (a) Cyclic voltammograms of the ATO-LTO composite electrode at a scan rate of 0.2mVs^{-1} for the first five cycles, (b) cyclic voltammograms of the ATO-LTO composite at different scan rates ranging from 0.2 mVs^{-1} to 5 mVs^{-1}; the inset shows the dependence of the anodic peak current on the square root of the scan rate, (c) typical charge-discharge curves of the ATO-LTO composite electrode for the first two cycles at a current density of 0.1 Ag^{-1}, (d) rate capability of the ATO-LTO composite anodes.

In the second cycle however, the discharge capacity is ~124 $mAhg^{-1}$ and the charge capacity is 110.5 $mAhg^{-1}$ which results in a much-improved coulombic efficiency of ~89%. **Fig. 4d** shows the rate capability of the ATO-LTO composite anode at different rates for a cycle step of 20 cycles. Discharge capacities of ca. 88 $mAhg^{-1}$, 77 $mAhg^{-1}$, 68 $mAhg^{-1}$, 57 $mAhg^{-1}$, 44 $mAhg^{-1}$, and 31 $mAhg^{-1}$, were noted at the last cycle for current rates of 0.1 Ag^{-1}, 0.2 Ag^{-1}, 0.4 Ag^{-1}, 0.8 Ag^{-1}, and 1.6Ag^{-1}, respectively. Furthermore, the composite exhibited good reversibility since all of the capacity was restored after the cell was cycled back from a high current rate of 3.2 Ag^{-1} to a low current rate of 0.1 Ag^{-1}.

***Li-HEC cell*:** The Li-HEC cell performance is depicted in **Fig. 5**. The cells were constructed after prelithiating the anode to a potential of 0.05V vs Li/Li$^+$ at a very low current rate of 0.05 Ag^{-1}. As noted by Zheng [**38**], organic electrolytes have relatively lower salt concentration as opposed to aqueous electrolytes and therefore the energy of the hybrid device can be limited by the electrolyte when a lithium intercalating anode is used. As the cell charges, the lithium ions are consumed at the negative electrode whereas the anions are adsorbed at the cathode. If the electrolyte were depleted of ions, the device cannot be charged further and as a solution, they proposed the utilization of a prelithiated anode, which could compensate for the electrolyte ion depletion [**39**]. The rGO-CNT electrodes, on the other hand were used for Li-HEC construction after full electrochemical activation, i.e. after ~100 cycles. As was noted in **Fig. 3b**, the discharge capacity of the rGO-CNT electrode increased steadily for the first ~60 cycles and then stabilized. Allowing the rGO-CNT electrode to activate before Li-HEC assembly ensured higher capacity utilization from the cathode.

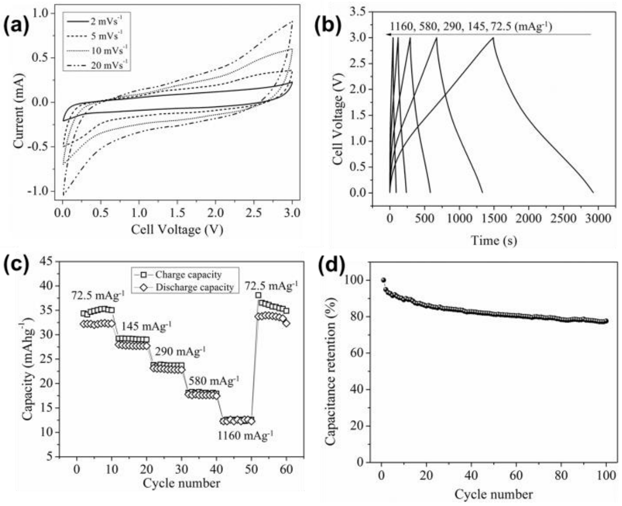

Fig. 5: (a) Cyclic voltammograms of the Li-HEC at different scan rates ranging from 2-20 mVs^{-1}, (b) typical charge-discharge curves of the Li-HEC cells at different current densities, (c) rate capability, and (d) cyclability of the Li-HEC full cells.

As noted in **Fig. 5a**, the shape of the CV curves of the Li-HECs is typical of capacitive behavior with a slight deviation, which could be a result of the composite charge storage characteristics arising from the predominantly redox-diffusion controlled lithium storage in the anode as opposed to the surface-dominated double layer charge adsorption in the cathode. The galvanostatic charge-discharge curves of the Li-HEC, displayed as **Fig. 5b**, are mostly triangular for a cell potential between a cell potential of 0.01-3.0V also indicative of capacitive behavior. The rate capability of the Li-HEC cell is shown in **Fig. 5c** - the full cell was able to deliver discharge capacities of 32.29 $mAhg^{-1}$, 27.70 $mAhg^{-1}$, 22.82 $mAhg^{-1}$, 17.45 $mAhg^{-1}$, and 12.27 $mAhg^{-1}$ for current rates of 72.5 mAg^{-1}, 145 mAg^{-1}, 290 mAg^{-1}, 580 mAg^{-1}, and 1160 mAg^{-1}, respectively. Moreover, the cell performance was very stable for a cycle step of 10 for the given current rate and all of the cell capacity is recovered after cycling from a high current rate of 1160 mAg^{-1} to 72.5 mAg^{-1}, which is indicative of good rate capability and reversibility of the full cell. **Fig. 5d** shows the capacitive retention of the Li-HEC full after 100 cycles; the cell was able to retain ~77% of the initial capacitance. The **Fig. 6** shows the Ragone chart of the Li-HEC cell based on discharge characteristics. The hybrid capacitor was able to deliver a maximum energy density of 33.35 $Whkg^{-1}$ and a maximum power density of 1207.4 Wkg^{-1}. All the cell parameters were normalized with the total anode and cathode active material masses. The range for the energy density was between 33.35-15.09 $Whkg^{-1}$ at power densities of 83.55-1207.4 Wkg^{-1}. The energy-power characteristics of the Li-HEC cells are superior to aqueous hybrid systems including RuO_2-TiO_2//AC [**40**], $LiTi_2(PO_4)_3$//AC [**41**] configurations, as well as comparable or even better than nonaqueous hybrid systems comprising modified LTO [**42-44**]. **Table 1** summarizes the electrochemical performance of this work along with some of the other hybrid capacitors reported in other reports. The superior energy-power characteristics are attributed to the utilization of an organic electrolyte, which allows for a wider stable electrochemical potential window (0.05-3V) and the porous morphology of the ESD generated rGO-CNT cathode, which is ideal for high power handling applications. It should be noted that this work combined a pristine lithium-intercalation based anode with a double layer counter cathode, categorically a "serial" system.

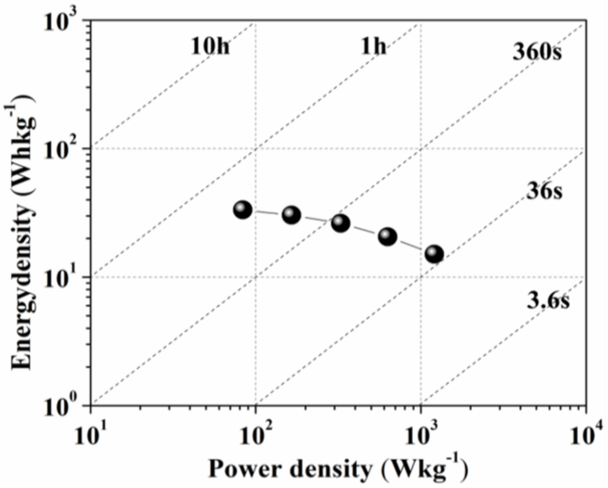

Fig. 6. Ragone Plot of the ESD-based Li-HEC full cells based on discharge characteristics.

Enhancement in energy-power characteristics is expected with the utilization of a "parallel" system. The combination of a redox based material and a double layer material within one electrode allows for intrinsic potential matching as the materials used have to be stable for the same voltage window [**1**]. Furthermore, the internal

Table 1. Comparison of the ESD based Li-HEC with other hybrid electrochemical capacitors.

Positive electrode	**Negative electrode**	**Electrolyte**	**Cell Voltage (V)**	**Capacitance (Fg^{-1})**	**Capacity ($mAhg^{-1}$)**	**Energy-power characteristics**	**Ref.**
RuO_2/TiO_2	AC	1M KOH (aqueous)	0-1.4V	46 Fg^{-1} at 130 $mAcm^{-2}$	-	12.5 $Whkg^{-1}$ at a power density of 150Wkg^{-1} 5.7 Wkg^{-1} at a power density of 1207 Wkg^{-1}	**40**
AC	Carbon-coated $LiTi_2(PO_4)_3$	1M Li_2SO_4 (aqueous)	0.3 to 1.5 V	-	30 $mAhg^{-1}$ at 2 $mAcm^{-2}$	24 Wh kg^{-1} at a power density of about 200 W kg^{-1} 15 Wh kg^{-1} at a power density of 1000 W kg^{-1}	**41**
Graphene sheets wrapped nano-$Li_4Ti_5O_{12}$	AC	1 M $LiPF_6$/EC/ DMC (nonaqueous)	1.5–3.0 V			29.2 Wh kg^{-1} at a power density of 58.4 W kg^{-1} 1782.7 W kg^{-1} , the specific energy retains 13.4 Wh kg^{-1}	**42**
AC	Carbon coated $Li_4Ti_5O_{12}$	1M $LiPF_6$ in propylene carbonate (nonaqueous)	1.5-2.5V		~30 $mAhg^{-1}$ at 0.17 Ag^{-1}	16$Whkg^{-1}$ at 1010 Wkg^{-1}	**43**
AC	Carbon modified $Li_4Ti_5O_{12}$	1-M LiPF6 in EC/DMC (1:3 in volume)	1.5-3.0V	83 Fg^{-1} at a current rate of 60 mAg^{-1}		16$Whkg^{-1}$ at 440 Wkg^{-1}	**44**
Reduced graphene oxide-carbon nanotube composite (rGO-CNT)	Anatase TiO_2-$Li_4Ti_5O_{12}$	1 M $LiPF_6$/EC/ DMC (nonaqueous)	0.05-3V	-	~32 $mAhg^{-1}$ at 0.1Ag^{-1}	33.35 $Whkg^{-1}$ at 83.55 Wkg^{-1} 26.2 $Whkg^{-1}$ at 327.5 Wkg^{-1} 15.09 $Whkg^{-1}$ at 1207.4 Wkg^{-1}	This work

parallel system mitigates the capacity mismatch arising from the disparate charge storage mechanism of the redox and double layer materials, and therefore helps in higher material utilization rate. In addition, improving the ionic and electronic conductivity of the electrodes is expected to further improve the Li-HEC performance. This work is still in nascent phase and as mentioned, much enhancement is expected with the use of an ESD based parallel system, which is a subject of future works.

Conclusion

A novel 3V Li-HEC utilizing ESD based rGO-CNT composite cathode and an anatase TiO_2-$Li_4Ti_5O_{12}$ anode was constructed and analyzed. The cathode and anode were first analyzed as working electrodes against a lithium counter electrode and were able to deliver discharge capacities of ca. 63 $mAhg^{-1}$ and 95 $mAhg^{-1}$ with good reversibility and cycling. The full Li-HEC cells were able to deliver a maximum energy density of 33.35 $Whkg^{-1}$ and a maximum power density of 1207.4 Wkg^{-1}, with specific energy ranging between 33.35-15.09 $Whkg^{-1}$ at power densities of 83.55-1207.4 Wkg^{-1}, where all the cell parameters were normalized with the total anode and cathode masses. Furthermore, the Li-HEC cells were able to retain ~77% of capacitance retention after 100 cycles. The superior energy-power cell characteristics are attributed to the porous electrode structure and the utilization of organic electrolyte which allows for a wider electrochemical potential window. The feasibility of using ESD for construction of a high performance hybrid capacitor was thus demonstrated in this report. Further enhancement in energy and power is expected with the use of ESD based internal parallel systems which can address voltage matching and mitigate double layer and redox charge storage mismatch, which are subjects of future works.

Acknowledgements

This work was partially supported by the National Science Foundation (NSF) projects (no. 1506640 and no. 1509735) and NERC ASSIST center seed funding. The authors would like to thank Dr. Yusuf Emirov for his kind help with TEM data procurement and analyses. R.A. and C.C. acknowledge the University Graduate School at Florida International University for support through Doctoral Evidence Acquisition (DEA) and Dissertation Year Fellowship (DYF), respectively. C.W. thanks Jilin University for Changbaishan Scholarship.

Author's contributions

Conceived the plan: CW, RA, CC; Performed the experiments: RA, CC; Data analysis: RA, CC, SD, CW; Wrote the paper: RA. Authors have no competing financial interests.

References

1. Cericola, D.; Kotz, R; *Electrochim. Acta*, **2012**, *72*, 1. **DOI:** 10.1016/j.electacta.2012.03.151
2. Amatucci, G. G.; Badway, F.; Pasquier, A. D.; Zheng, T; *J. Electrochem. Soc.*, **2001**, *148*, A930. **DOI:** 10.1149/1.1383553
3. Sivakkumar, S. R.; Milev, A. S.; Pandolfo, A. G.; *Electrochim. Acta*, **2011**, *56*, 9700. **DOI:** 10.1016/j.electacta.2011.06.060
4. Sivakkumar, S. R.; Nerkar, J. Y.; Pandolfo, A. G.; *Electrochim. Acta*, **2010**, *55*, 3330. **DOI:** 10.1016/j.electacta.2010.01.059
5. Agrawal, R.; Hao, Y.; Song, Y.; Chen, C.; Wang, C.; *Proc. SPIE 9493*, Energy Harvesting and Storage: Materials, Devices, and Applications VI, 94930B, **2015.**
6. Naoi, K; Naoi, W; Aoyagi, S.; Miyamoto, J.; Kamino, T.; *Acc. Chem. Res.*, **2013**, *46*, 1075. **DOI:** 10.1021/ar200308h
7. Ping, L.; Zheng, J.; Shi, Z.; Qi, J.; Wang C. Y.; *Chin. Sci. Bull.*, **2013**, *58*, 689. **DOI:** 10.1007/s11434-012-5456-9
8. Li, J.; Zhang, X; Peng, R.; Huang, Y.; Guo, L.; Qi, Y. C.; *RSC Adv.*, **2016**,*6*, 54866. **DOI:** 10.1039/C6RA09103B
9. Byeon, A.; Boota, M.; Beidaghi, M.; Aken, K. V.; Lee, J. W.; Gogotsi, Y.; *Electrochem. Commun.*, **2015**, *60*, 199. **DOI:** 10.1016/j.elecom.2015.09.004
10. Brousse, T.; Marchand, R.; Taberna, P. L.; Simon, P.; *J. Power Sources*, **2006**, *158*, 571. **DOI:** 10.1016/j.jpowsour.2005.09.020
11. Hsieh, C. L.; Tsai, D. S.; Chiang, W. W.; Liu, Y. H.; *Electrochim. Acta*, **2016**, *209*, 332. **DOI:** 10.1016/j.electacta.2016.05.090
12. Tu, F. Y.; Liu; S. Q.; Wu, T. H.; Jin, G. H.; Pan, C. Y.; *Powder Technology*, **2014**, *253*, 580. **DOI:** 10.1016/j.powtec.2013.12.008
13. Agrawal, R.; Chen, C.; Hao, Y.; Song, Y.; Wang, C. “Graphene for Supercapacitors”, In Graphene-Based Energy Devices; Yusoff, A. R. B. M. (Ed.); Wiley-VCH: Weinheim, **2015**, pp 171. **DOI:** 10.1002/9783527690312.ch6
14. Beidaghi, M.; Wang, C.; *Adv. Funct. Mater.*, **2012**, *22*, 4501. **DOI:** 10.1002/adfm.201201292
15. Jung, N.; Kwon, S.; Lee, D.; Yoon, D. M.; Park, Y. M.; Benayad, A.; Choi, J. Y.; Park, J. S.; *Adv. Mater.*, **2013**, *25*, 6854. **DOI:** 10.1002/adma.201302788
16. Agrawal, R., Nieto, A., Chen, H., Mora, M., Agarwal, A., *ACS Appl. Mater. Interfaces*, **2013**, *5*, 12052. **DOI:** 10.1021/am4038678
17. Froschl, T.; Hormann, U.; Kubiak, P.; Kucerova, G.; Pfanzelt, M.; Weiss, C. K.; Behm, R. J.; Huesing, N.; Kaiser, U.; Landfester, K.; Wohlfahrt-Mehrens, M.; *Chem Soc Rev*, **2012**, *41*, 5313. **DOI:** 10.1039/c2cs35013k
18. Yi, T. F.; Yang, S. Y.; Xie, Y.; *J. Mater. Chem. A*; **2015,** *3*, 5750. **DOI:** 10.1039/c4ta06882c
19. Chen, J. S.; Lou, X. W.; *Electrochem. Commun.*, **2009**, *11*, 2332. **DOI:** 10.1016/j.elecom.2009.10.024
20. Deng, D.; Kim, M. G.; Lee, Y. L.; Cho, J.; *Energy Environ. Sci.*, **2009**, *2*, 818. **DOI:** 10.1039/b823474d
21. Gao, L.; Li, S.; Huang, D.; Shen, Y.; Wang, M.; *J. Mater. Chem. A*; **2015**, *3*, 10107. **DOI:** 10.1039/C5TA01054C
22. Wang, J.; Zhao, H.; Yang, Q.; Wang, C., Lv, P.; Xia, Q.; *J. Power Sources*, **2013**, *222*, 196. **DOI:** 10.1016/j.jpowsour.2012.08.082
23. Yi, T.; Fang, Z.; Xie, Y.; Zhu, Y.; Yang, S.; *ACS Appl. Mater. Interfaces*, **2014**, *6* (22), 20205. **DOI:** 10.1021/am5057568
24. Jaworek, A.; Sobczyk, A.T.; Krupa, A.; Lackowski, M.; Czech. T.; *Bull. Pol. Acad. Sci., Tech. Sci*, **2009**, *57*, 63. **DOI:** 10.2478/v10175-010-0106-3
25. Jaworek, A.; Sobczyk, A.T.; *J Electrostat*, **2008**, *66*, 197. **DOI:** 10.1016/j.elstat.2007.10.001
26. Chen, C.; Agrawal, R.; Kim, T. K.; Li, X.; Chen, W.; Yu, Y.; Beidaghi, M.; Penmatsa, V.; Wang, C.; ECS Trans., 2014, *61*, 155. **DOI:** 10.1149/06127.0155ecst
27. Li, X.; Wang, C.; Mater. Chem. A, **2013**, *1*, 165. **DOI:** 10.1039/c2ta00437b
28. Sokolov, S.; Paul, B.; Ortel, E.; Fischer, A.; Kraehnert, R.; Langmuir, **2011**, *27*, 1972. **DOI:** 10.1021/la104272h
29. Dhanabalan, A.; Li, X.; Agrawal, R.; Chen, C.; Wang, C.; Nanomaterials, **2013**, *3*, 606. **DOI:**10.3390/nano3040606

30. Beidaghi, M.; Wang, Z.; Gu, L.; Wang, C.; J Solid State Electrochem, **2012**, *16*, 3341.
DOI: 10.1007/s10008-012-1777-5
31. Rattana, T.; Chaiyakun, S.; Witit-anun, N.; Nuntawong, N.; Chindaudom, P.; Oaew, S.; Kedkeaw, C.; Limsuwan, P.; *Procedia Engineering*, **2012**, *32*, 759.
DOI: 10.1016/j.proeng.2012.02.009
32. González, M. G.; Cabanelas, J. C.; Baselga, J. Applications of FTIR on Epoxy Resins - Identification, Monitoring the Curing Process, Phase Separation and Water Uptake, In Infrared Spectroscopy - Materials Science, Engineering and Technology; Theophanides, T. (Ed.); InTech
DOI: 10.5772/36323
33. Sim, L. C.; Leong, K. H.; Ibrahim, S.; Saravanan, P.; *J. Mater. Chem. A*, **2014**, *2*, 5315.
DOI: 10.1039/C3TA14857B
34. Kim, H.; Park, K. Y.; Hong, J.; Kang, K.; *Sci. Rep.*, **2014**, *4*, 5278.
DOI:10.1038/srep05278
35. Batchelor-McAuley, C.; Compton, R. G.; *J. Electroanal. Chem.*, **2012**, *669*, 73.
DOI:10.1016/j.jelechem.2012.01.016
36. Sun, J.; Teng, D.; Liu, Y.; Chi, C.; Yu, Y.; Lan, J. H.; Yang, X.; *RSC Adv.*, **2014**, *4*, 48632.
DOI: 10.1039/C4RA08501A
37. Gao, L.; Huang, D.; Shen, Y.; Wang, M.; *J. Mater. Chem. A*; **2015**, *3*, 23570.
DOI: 10.1039/C5TA07666H
38. Zheng, J. P.; *J. Electrochem. Soc.*, **2003**, *150*, A484.
DOI: 10.1149/1.1559067
39. Zheng, J. P.; *J. Electrochem. Soc.*, **2009**, *156*, A500.
DOI: 10.1149/1.3121564
40. Wang, Y. G., Wang, Z.; Xia, Y.; *Electrochim. Acta*, **2005**, *50*, 5641.
DOI:10.1016/j.electacta.2005.03.042
41. Luo, J. Y.; Xia, Y.; *J. Power Sources*, **2009**, *186*, 224.
DOI:10.1016/j.jpowsour.2008.09.063
42. Yuan, T.; Li, W. T.; Zhang, W.; He, Y. S.; Zhang, C.; Liao, X. Z.; Ma, Z. F.; *Ind. Eng. Chem. Res.*, **2014**, *53*, 10849.
DOI: 10.1021/ie501287a
43. Jung, H. G.; Venugopal, N.; Scrosati, B.; Sun, Y. K.; *J. Power Sources*, **2013**, *221*, 266.
DOI: 10.1016/j.jpowsour.2012.08.039
44. Ni, J.; Yang, L.; Wang, H.; Gao, L.; *J. Solid State Electrochem*, **2012**, *16*, 2791.
DOI: 10.1007/s10008-012-1704-9